

# PCCP

Accepted Manuscript

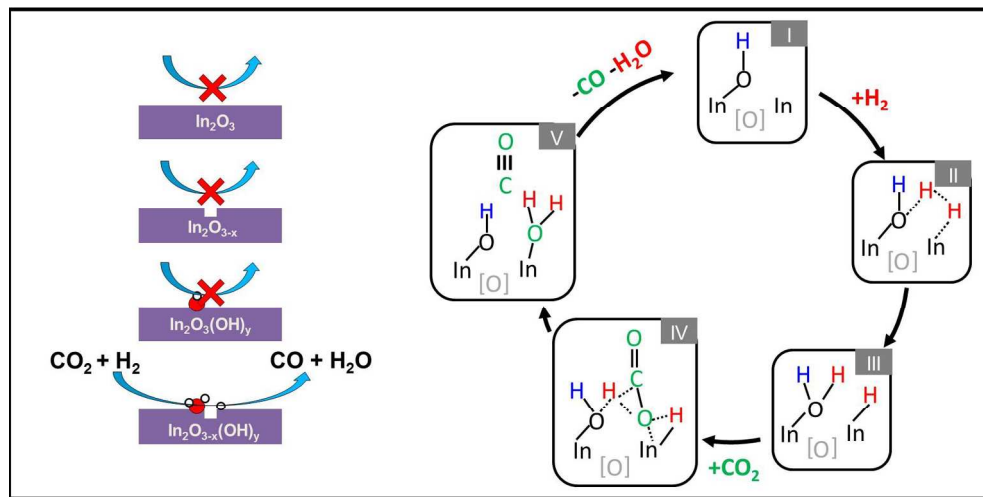


This is an *Accepted Manuscript*, which has been through the Royal Society of Chemistry peer review process and has been accepted for publication.

*Accepted Manuscripts* are published online shortly after acceptance, before technical editing, formatting and proof reading. Using this free service, authors can make their results available to the community, in citable form, before we publish the edited article. We will replace this *Accepted Manuscript* with the edited and formatted *Advance Article* as soon as it is available.

You can find more information about *Accepted Manuscripts* in the [Information for Authors](#).

Please note that technical editing may introduce minor changes to the text and/or graphics, which may alter content. The journal's standard [Terms & Conditions](#) and the [Ethical guidelines](#) still apply. In no event shall the Royal Society of Chemistry be held responsible for any errors or omissions in this *Accepted Manuscript* or any consequences arising from the use of any information it contains.



500x250mm (96 x 96 DPI)

## ARTICLE

# Illuminating CO<sub>2</sub> Reduction: Investigating the Role of Surface Hydroxides and Oxygen Vacancies on Nanocrystalline In<sub>2</sub>O<sub>3-x</sub>(OH)<sub>y</sub>

Cite this: DOI: 10.1039/x0xx00000x

Received 00th January 2012,  
Accepted 00th January 2012

DOI: 10.1039/x0xx00000x

[www.rsc.org/](http://www.rsc.org/)Kulbir Kaur Ghuman<sup>a,†</sup>, Thomas E. Wood<sup>b,†</sup>, Laura B. Hoch<sup>c</sup>, Charles A. Mims<sup>b</sup>, Geoffrey A. Ozin<sup>c</sup> and Chandra Veer Singh<sup>a</sup>

Designing catalytic nanostructures that can thermochemically or photochemically convert gaseous carbon dioxide into carbon based fuels is a significant challenge, which requires a keen understanding of the chemistry of reactants, intermediates and products on surfaces. In this context, it has recently been reported that the reverse water gas shift reaction (RWGS), whereby carbon dioxide is reduced to carbon monoxide and water,  $\text{CO}_2 + \text{H}_2 \rightarrow \text{CO} + \text{H}_2\text{O}$ , can be catalysed by hydroxylated indium oxide nanocrystals, denoted  $\text{In}_2\text{O}_{3-x}(\text{OH})_y$ , more readily in the light than in the dark. The surface hydroxide groups and oxygen vacancies on  $\text{In}_2\text{O}_{3-x}(\text{OH})_y$  were both shown to assist this reaction. While this advance provided a first step towards the rational design and optimization of a single-component gas-phase CO<sub>2</sub> reduction catalyst for solar fuels generation, the precise role of the hydroxide groups and oxygen vacancies in facilitating the reaction on  $\text{In}_2\text{O}_{3-x}(\text{OH})_y$  nanocrystals has not been resolved. In the work reported herein, for the first time we present *in situ* spectroscopic and kinetic observations, complemented by density functional theory analysis, that together provide mechanistic information into the surface reaction chemistry responsible for the thermochemical and photochemical RWGS reaction. Specifically, we demonstrate photochemical CO<sub>2</sub> reduction at a rate of 150  $\mu\text{mol g}_{\text{cat}}^{-1} \text{hour}^{-1}$ , which is four times better than the reduction rate in the dark, and propose a reaction mechanism whereby a surface active site of  $\text{In}_2\text{O}_{3-x}(\text{OH})_y$ , composed of a Lewis base hydroxide adjacent to a Lewis base indium, together with an oxygen vacancy, assists the adsorption and heterolytic dissociation of H<sub>2</sub> that enables the dissociation and reaction of CO<sub>2</sub> to form CO and H<sub>2</sub>O as products. This mechanism, which has its analogue in molecular frustrated Lewis pair (FLP) chemistry and catalysis of CO<sub>2</sub> and H<sub>2</sub>, is supported by preliminary kinetic investigations. The results of this study emphasize the importance of engineering the surfaces of nanostructures to facilitate gas-phase thermochemical and photochemical carbon dioxide reduction reactions to energy rich fuels at technologically significant rates.

## 1.0 Introduction

Solar energy is an abundant source of sustainable energy which if harvested globally could satisfy both environmental challenges and growing energy demands.<sup>1,2</sup> Currently solar energy is harvested by wind, solar-thermal and photovoltaic technologies. However, a global paradigm shift is currently underway where the greenhouse gas CO<sub>2</sub> is regarded as chemical feedstock for a carbon neutral sustainable energy economy.<sup>3-5</sup> This has led to the pursuit of new technologies, which aim to capture light energy in the form of chemical energy through the generation of solar fuels from CO<sub>2</sub>.<sup>6-8</sup> Converting CO<sub>2</sub> energy production and manufacturing exhaust streams into valuable products (such as hydrocarbon fuels or

chemical feed stocks) addresses both climate change and energy security.<sup>9</sup>

Technologies, such as the artificial leaf, are multi-component systems where absorbed light generates electron/hole pairs which are capable of redox reactions on a photocatalyst's surface.<sup>1,10</sup> However, an archetypical design has yet to be established. The complex chemistry arises from the redox chemistry which is a multi-electron / multi-hole process that requires significantly high potentials to drive the reaction. For example, photosynthetic methanol production is a six electron process with a Gibbs's Free energy of reaction of 707 kJ mol<sup>-1</sup>. This poses a significant challenge which can be addressed by finding materials capable of facilitating a specific part of the overall process.

An artificial leaf can be considered to have four major components, a reduction catalyst, an oxidation catalyst, a proton conductor and an electron conductor. While significant advances have been made in water splitting with production rates of  $1 \text{ mmol g}_{\text{cat}}^{-1} \text{ hr}^{-1}$ , photocatalytic  $\text{CO}_2$  activation has stagnated around  $1 \mu\text{mol g}_{\text{cat}}^{-1} \text{ hr}^{-1}$ .<sup>8</sup> Since activation of  $\text{CO}_2$  by solar light is necessary for the production of solar fuels like  $\text{CO}$ ,  $\text{CH}_4$ ,  $\text{CH}_3\text{OH}$ ,  $\text{HCOOH}$  etc., there is growing interest in the research community to discover and study materials that can use light energy efficiently to activate gaseous  $\text{CO}_2$  into different carbon based chemical products.<sup>11,12</sup> A photocatalyst capable of  $\text{CO}_2$  reduction could be combined in series with a water splitting system which produces  $\text{H}_2$  sustainably, or it may be incorporated into a multi-component cell. Careful investigation of  $\text{CO}_2$  activation on surfaces may provide insight for designing materials that will power these solar fuel technologies in the future.

Indium sesquioxide ( $\text{In}_2\text{O}_3$ ) is increasingly capturing the attention of researchers as a potential photocatalyst due to its favourable optical, electronic and surface properties.<sup>13–17</sup> Among many n-type transparent conducting metal oxides (TCOs) like  $\text{ZnO}$ ,  $\text{CdO}$  and  $\text{SnO}$ ,  $\text{In}_2\text{O}_3$  is one of the most widely used n-type TCO due to its combination of a large optical band gap and low electrical resistivity.<sup>18–20</sup> After the revision of the bandgap value of  $\text{In}_2\text{O}_3$ , it was realized that electron accumulation on its surfaces can be achieved with low bulk doping levels.<sup>21</sup> Moreover  $\text{In}_2\text{O}_3$  is also very stable under illumination as compared to other kinds of semiconductors, such as metal sulfides. These properties make it a suitable candidate for electronic and photocatalytic applications. There have been several investigations reported since then for its use in electronic device applications.<sup>22–27</sup> However, very little has been reported on the photocatalytic activity of indium oxide so far. Recently our group has demonstrated light-assisted, gas-phase photoreduction of  $\text{CO}_2$  to  $\text{CO}$  over hydroxylated  $\text{In}_2\text{O}_{3-x}(\text{OH})_y$  nanocrystals at rates as high as  $15 \mu\text{mol g}_{\text{cat}}^{-1} \text{ hour}^{-1}$  in  $\text{H}_2$  atmospheres at  $150^\circ\text{C}$  via the reverse water gas shift (rWGS) reaction. The high photoactivity was attributed to surface hydroxide groups and oxygen vacancies, whose relative concentration correlated well with the  $\text{CO}_2$  adsorption capacity and  $\text{CO}$  production rate. This remarkable observation suggested that both surface hydroxide groups and oxygen vacancies play a vital role in the reaction mechanism; however their function was unclear at the time.<sup>28</sup> Thus, it became apparent that a fundamental understanding of the function of the hydroxide groups and oxygen vacancies on the surface of  $\text{In}_2\text{O}_{3-x}(\text{OH})_y$  nanocrystals will prove to be pivotal for the rational design of advanced catalysts for the activation of  $\text{CO}_2$  in the future.

Motivated by this challenge, we describe herein a combined spectroscopic, kinetic and density functional theory study designed to provide an insight into the effect of surface hydroxide groups and oxygen vacancies on the RWGS reaction mechanism. The combined experimental and theoretical results support a mechanism in which  $\text{CO}_2$  is adsorbed on the  $\text{In}_2\text{O}_{3-x}(\text{OH})_y$  surface at an active site, which arises from the heterolytic splitting of  $\text{H}_2$  on adjacent hydroxide and indium

sites which are next to a surface oxygen vacancy. Proton and hydride transfer to adsorbed  $\text{CO}_2$  subsequently leads to the production of  $\text{CO}$  and  $\text{H}_2\text{O}$  with concomitant regeneration of the hydroxides and oxygen vacancies. This site is analogous to a frustrated Lewis pair (FLP) site an exciting new discovery for surface chemistry on semiconductors. The proposed mechanism, with emphasis on the identified active site, will open the way for improved material selection and design of surfaces capable of reducing  $\text{CO}_2$  for sustainable energy production devices.

## 2.0 Methodology

### 2.1. Computational model

The spin-polarized calculations were performed by the Perdew-Burke-Ernzerhof (PBE) exchange-correlation functional within the generalized gradient approximation (GGA) and the Rappe-Rabe-Kaxiras-Joannopoulos (RRKJ) ultra-soft pseudopotentials implemented in the Quantum Espresso software.<sup>29–31</sup> Kinetic energy cut-offs of 50 and 200 Ry were used for the wavefunctions and charge density, respectively and the self-consistent field convergence criterion was set to  $1\text{E}^{-6}$  Ry. Each system was relaxed with variable cell size using conjugate gradient minimization until the magnitude of the residual Hellman-Feynman force on each atom was less than  $1\text{E}^{-3}$  Ry/Bohr. Based on experimental evidence, density functional theory (DFT) calculations were conducted for the (111) surface in the present study. Notably, this surface is also the most abundant crystal face from a thermodynamic equilibrium perspective.<sup>32</sup> To model the  $\text{In}_2\text{O}_3$  (111) surface, a 4-layer slab having 160 atoms was used, in which a vacuum layer of  $\sim 20\text{\AA}$  was applied. The modelled system was a continuous layer, roughly  $11.5\text{\AA}$  in thickness, which represents a nanofilm, and captures the behaviour of non-edge nanocrystal regions which form the majority of surface area. In all calculations, the bottom two layers were frozen at their equilibrium bulk positions, whereas the top two layers together with the adsorbates were allowed to relax. Because of the large size of the supercell, Brillouin zone integrations were performed using the gamma k-point only. The complicated surface with low symmetry is shown in Fig. 1E, while a side view of the supercell is shown in Fig. 1D. Bader charge analyses were performed for pristine and defected  $\text{In}_2\text{O}_3$  (111) surfaces with and without  $\text{CO}_2$  adsorption.<sup>33,34</sup> Transition states (TS) along a minimum energy reaction path (MEPs) were determined using the climbing image nudged elastic-band (CI-NEB) method with 11 images.<sup>35–37</sup>

### 2.2. Material synthesis and characterization

Nanocrystalline  $\text{In}_2\text{O}_{3-x}(\text{OH})_y$  powder used in this work was synthesised by thermal treatment of  $\text{In}(\text{OH})_3$  nanocrystals at  $250^\circ\text{C}$  for 3 hours. A detailed description of the synthesis of the  $\text{In}(\text{OH})_3$  precursors and characterization of the  $\text{In}_2\text{O}_{3-x}(\text{OH})_y$  is outlined in a previous work.<sup>28</sup> The nanocrystals morphology

was determined using a JEOL-2010 high resolution transmission electron microscope (HR-TEM). Powder X-ray diffraction (PXRD) was performed on a Bruker D2-Phaser X-ray diffractometer, using Cu K $\alpha$  radiation at 30 kV.

### 2.3. Photocatalytic measurements and surface characterization

The gas-phase photocatalytic rate measurements were carried out in a packed flow reactor. A borosilicate tube (3 mm outer diameter and 2.5 mm inner diameter) was packed with 20 mg (1 cm catalyst bed length) of  $\text{In}_2\text{O}_{3-x}(\text{OH})_y$  nanocrystal powder, with quartz wool as support at both ends. The tubular reactor was heated by conduction using a heated copper block from below as shown in Fig. 2. The reactor was fastened within a custom fabricated stainless steel brace which suspends the reactor within a channel of a heated copper block, allowing heating from the sides and below. The top of the reactor was exposed to light irradiation from a Newport 300 W Xe lamp at a distance of 2 cm, with a light intensity of  $1000 \text{ W m}^{-2}$ . Reaction gas mixtures were composed of  $\text{H}_2$  (99.9995%),  $\text{CO}_2$  (99.9999%) and an inert He (99.9999%). In order to stimulate

different reaction conditions, either the total volumetric flow rate was varied ranging from 5 to 15 mL/min, or each gas was varied while maintaining a constant flow rate. The reactor temperatures were controlled by an OMEGA CN616 6-Zone temperature controller combined with a thermocouple placed at the top of the catalyst bed within the reactor. Pressure indicators were installed at the inlet and the outlet of the reactor to monitor the pressure drop across the catalyst bed. The heating program increased the set point with  $10^\circ\text{C}$  temperature intervals, with a specific temperature maintained for a 40 minute time interval before increasing it to the next set point with a ramp rate of  $1^\circ\text{C min}^{-1}$ . The product gases in the outlet stream of the reactor were analysed with an 8610 gas chromatograph (SRI) installed with a 1' Mol Sieve 5a column and a 6' Haysep D column.

*In-situ* diffuse reflectance infrared spectroscopy (DRIFTS) measurements were conducted using a Harrick Praying Mantis diffuse reflectance chamber with a Harrick environmental chamber. Powdered nanocrystalline  $\text{In}_2\text{O}_{3-x}(\text{OH})_y$  was packed into the sample cup and installed into the sample chamber. A reference spectrum was obtained after the powder had been

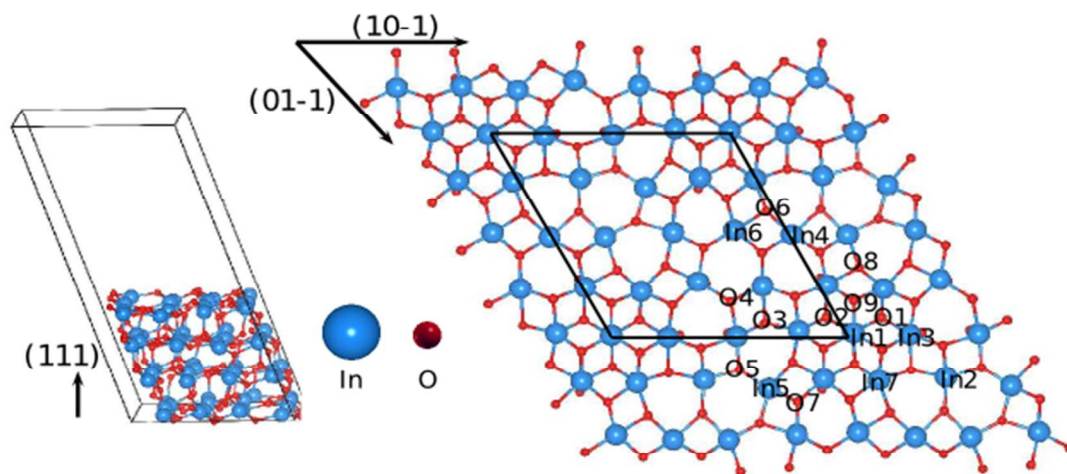
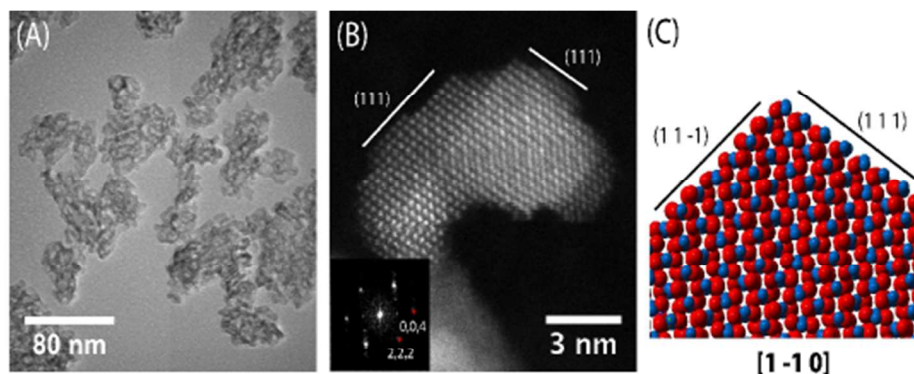
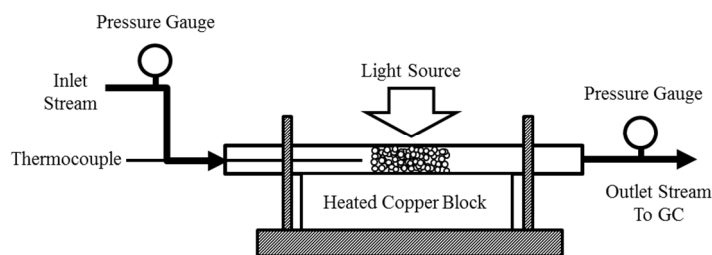


Fig  
sam  
cori

with cuts along the (111) and (11-1) planes. (D) Side view of nanocrystalline  $\text{In}_2\text{O}_3$  supercell with (111) orientation. (E) The upper surface structure of (111) terminated  $\text{In}_2\text{O}_3$ . Surface In atoms (marked In#, where # = 1 to 7) and O atoms (marked O#, where # = 1 to 9) shown in (E) are considered for adsorption of various adsorbents. Red balls represent O atoms while blue balls represent In atoms.

## ARTICLE

heated to 120°C in H<sub>2</sub> flowing at 20 cm<sup>3</sup> min<sup>-1</sup> for an hour, so as to remove any water or absorbed species. In order to obtain a reference spectrum, the chamber/powder was cooled to room temperature, and He was flowed through the chamber at 20 cm<sup>3</sup> min<sup>-1</sup> for an hour. Light irradiation was passed through the ZeSe window on the Harrick environmental chamber *via* an optical fibre of 1 meter in length attached to a Newport 300 W Xe Lamp with a light intensity of 200 W/m<sup>2</sup> at the end of the optical fibre.



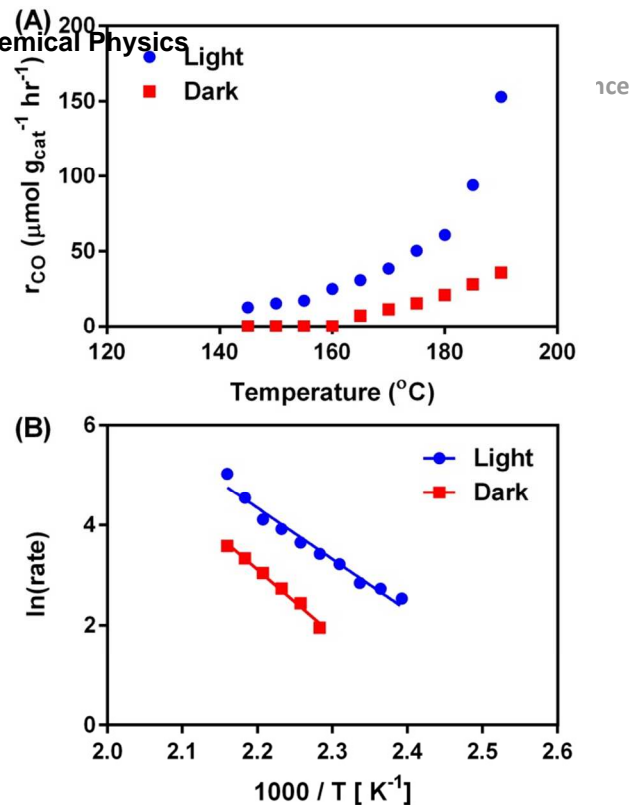
### 3.0 Results and discussion

We selected the most active sample of the nanocrystalline catalyst from our previous study and conducted its morphological characterization.<sup>12</sup> The TEM image in Fig. 1A shows the overall morphology of the sample, indicating its porous nanocrystalline nature and high surface area, both necessary parameters for an active catalyst. The dark field HR-STEM image (Fig. 1B) illustrates the high crystallinity of the In<sub>2</sub>O<sub>3-x</sub>(OH)<sub>y</sub> sample. The fast Fourier transform (FFT) of the image, shown in the inset, corresponds to the (1-10) zone axis and allows for identification of the (111) surfaces indicated in the figure. The simulated structure used for DFT calculations is shown in Fig. 1D. It corresponds well with the experimental observations (Fig. 1A-C), and is focused solely on (111) surface of indium sesquioxide.

#### 3.1 Temperature dependence of CO production

In our previous work, the production rates of CO, measured in batch photoreactors for both thermochemical and photochemical conditions on In<sub>2</sub>O<sub>3-x</sub>(OH)<sub>y</sub> nanocrystals increased with temperature. However, the study was limited to a maximum operating temperature of 170°C.<sup>28</sup> Expanding upon our investigation of this material, the temperature dependence of the thermochemical and photochemical production of CO from CO<sub>2</sub> and H<sub>2</sub> on In<sub>2</sub>O<sub>3-x</sub>(OH)<sub>y</sub> nanocrystals was investigated in a flow reactor under various flowing gas atmospheres and in the dark and light, with the results shown in Fig. 3A. The In<sub>2</sub>O<sub>3-x</sub>(OH)<sub>y</sub> nanocrystals selected for this study were the nanocrystals with the highest CO<sub>2</sub> capture capacity and CO photocatalytic production from our previous study. The reaction was carried out in a flow reactor which is capable of higher

Fig. 2 Schematic diagram of the packed bed photoreactor



temperatures than previously possible in the batch photoreactors. At 290°C a CO production rate of 16.8 mmol g<sub>cat</sub><sup>-1</sup> hour<sup>-1</sup> was observed under irradiation. However, while

Fig. 3 (A) Temperature dependence of CO production for In<sub>2</sub>O<sub>3-x</sub>(OH)<sub>y</sub> nanoparticle catalysts under flowing H<sub>2</sub> and CO<sub>2</sub>. (B) Pseudo-Arrhenius plots drawn from temperature dependent measurements

heating to 300°C is possible, the catalyst did not appear to be stable in our work at temperatures above 200°C, due to sintering of the nanoparticles above 200°C and loss of surface hydroxides above 250°C, which limited investigations to temperatures up to 190°C.

Under light irradiation and flowing H<sub>2</sub> and CO<sub>2</sub>, reasonable photoactivity of 15.4 μmol g<sub>cat</sub><sup>-1</sup> hour<sup>-1</sup> is demonstrated at temperatures as low as 150°C, which increases to 153 μmol g<sub>cat</sub><sup>-1</sup> hour<sup>-1</sup> at 190°C. In the dark, while measurable CO production was not observed until 165°C, it increases to 35.7 μmol g<sub>cat</sub><sup>-1</sup> hour<sup>-1</sup> at 190°C under flowing H<sub>2</sub> and CO<sub>2</sub> conditions. We did not observe any other hydrocarbon products. Assuming that the apparent reaction rate constant, *k*, is proportional to the CO production rate, a pseudo-Arrhenius plot was prepared to estimate the apparent activation energy of both the thermochemical and photochemical reactions, as shown in Fig. 3B. The apparent activation energy of the photochemical RWGS reaction was estimated to be 86 kJ mol<sup>-1</sup> while for the thermochemical reaction it was estimated to be 107 kJ mol<sup>-1</sup>. This difference between light and dark activation energies amounts to 0.26 eV which results in an observed 4-fold increase in reaction rate due to photoactivation. Previous

studies reported activation energies of 40 kJ mol<sup>-1</sup> or less for photocatalytic reactions, where it was suggested this barrier arose from a physical step involving the adsorption or desorption of reactants or products; however, in this study the estimated activation energy is above 80 kJ mol<sup>-1</sup> suggesting a chemical reaction step may be the rate determining step.<sup>36,38</sup> It

chemical reaction steps, a lower photochemical activation energy compared to the thermochemical one is consistent with previous reports and will be the subject of future investigations.<sup>39,40</sup>

### 3.2 Kinetic Investigations

In order to gain insight into the reaction pathway we conducted kinetic measurements through the variation of key reaction parameters. These dependences were investigated both in presence and absence of light. The CO production rate was measured in the flow reactor, while varying (1) the flow rates for CO<sub>2</sub> and an inert diluent (He), (2) the flow rates for H<sub>2</sub> and an inert diluent (He) and (3) the total reactant flow rate, also characterized as a space velocity (volumetric flow rate divided by reactor volume). The temperature was chosen as 190°C for this particular study because of (i) the high CO production rate and (ii) the stability of In<sub>2</sub>O<sub>3-x</sub>(OH)<sub>y</sub> nanocrystals over a 10 hour reaction period under light reaction conditions, as shown in Fig. S1 contained in the Supporting Information.

Assuming that the reaction follows basic power law kinetics, the rate of CO production,  $r_{CO}$ , (rate per mass of catalyst) can be related to the partial pressure of each reactant and product as:

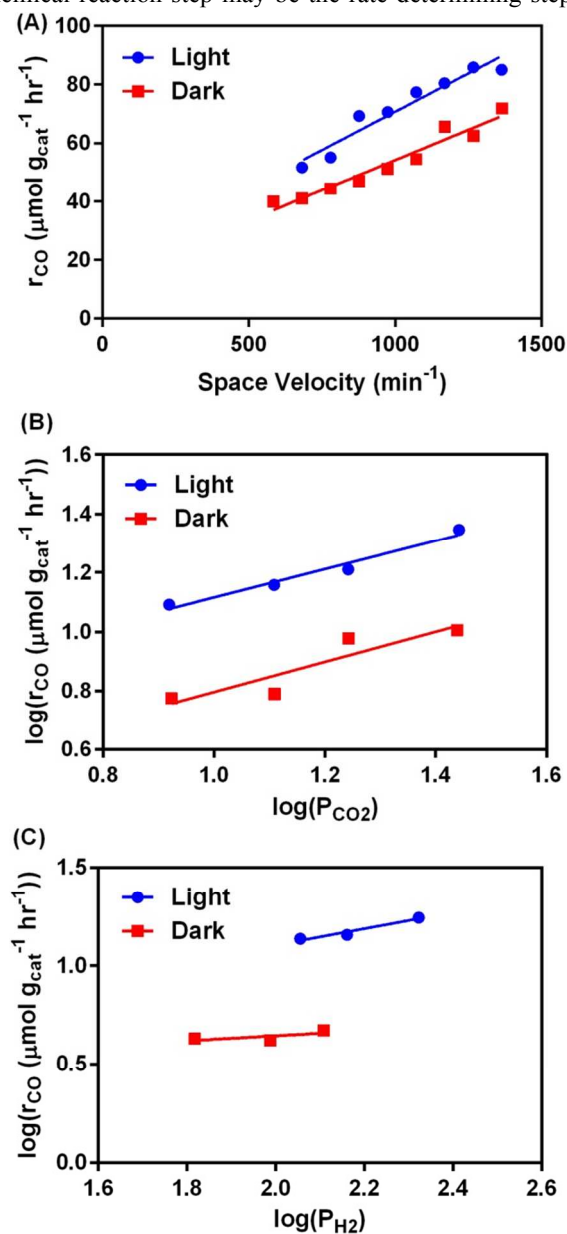
(1)

In expression (1),  $k_I$  is the rate constant;  $p_i$  is the partial pressure of reactant  $i$ ;  $\alpha$ ,  $\beta$ ,  $\gamma$ ,  $\delta$  are the reaction orders of H<sub>2</sub>, CO<sub>2</sub>, H<sub>2</sub>O, CO, respectively.  $r_{CO} = k_I p_{H_2}^\alpha p_{CO_2}^\beta p_{H_2O}^\gamma p_{CO}^\delta$

First, the dependence of the CO production rate on the space velocity was carried out. The space velocity, at constant inlet compositions, was varied under both light and dark conditions. As shown in Fig. 4A, the CO production rate decreases with decreasing space velocity under both light and dark conditions. This observed behaviour is consistent with a reaction product inhibiting the rate of reaction, since lower space velocity (longer gas residence time) allows a build-up of higher product concentrations. This hypothesis was tested using a simple plug flow reactor model and by assuming, once again, a power law kinetic expression and low conversion of the reactants. Here, we use a rate law which has a first order inhibition by one of the products, H<sub>2</sub>O in this case, i.e.

(2)

In expression (2),  $k_0$  is a rate coefficient for a given condition where the partial pressures of CO<sub>2</sub> and H<sub>2</sub> remain constant. A detailed description of this analysis is included in the Supplementary Information. The resulting expression, equation (3), predicts that the CO production rate is



is likely that the rate determining step for this reaction is the dissociation of CO<sub>2</sub>, which is predicted by theory and expected based on literature reports. We can speculate that the photoexcited electrons assist in this step. While it is not clear what the photochemical activation energy represents in terms of

Fig. 4 Rate law measurements for CO production from CO<sub>2</sub> and H<sub>2</sub> in the dark and light on In<sub>2</sub>O<sub>3-x</sub>(OH)<sub>y</sub> nanocrystals: (A) Dependence on space velocity (B) Dependence on the partial pressure of CO<sub>2</sub> (C) Dependence on the partial pressure of H<sub>2</sub>.

proportional to the half power of the relevant kinetic parameters, as observed:

$$F_{CO} = (2m_{cat}k_0(F_{TOT}/P_{TOT}))^{1/2} \quad (3)$$

In expression (3),  $F_{CO}$  (nmol  $hr^{-1}$ ) is the molar flow rate of CO,  $m_{cat}$ (g) is the weight of catalyst in the fixed bed, and  $F_{TOT}$ , the total molar flow rate, is proportional to the total volumetric flow rate (space velocity). When compared to the observed CO production rate plotted against the space velocity (see Fig. 4A), it is clear that under both dark and light condition, the reaction is inhibited by the products. Since it is expected that  $H_2O$  can inhibit the reaction by blocking oxygen vacancies and/or hydroxide groups on the  $In_2O_{3-x}(OH)_y$  surface, further investigations were carried out under both batch and flow reaction conditions to test this hypothesis. It was found that when  $H_2O$  is introduced into the reactor in the inlet stream, the CO production is significantly suppressed. Since the reaction conversion is far from equilibrium conversion ( $H_2$  and  $CO_2$  concentrations are little changed), it is clear that this result arises from inhibition by the water product. This result provides strong support for the RWGS reaction mechanism proposed by theoretical calculations, as detailed later in Section 3.5.

The effective order of the reaction for  $CO_2$  is determined by measuring the reaction rate while varying the partial pressure of  $CO_2$  and keeping the total flow rate and  $H_2$  partial pressure constant. Fig. 3B shows that the CO production rate, under both light and dark conditions, depends on the half power of the  $CO_2$  partial pressure. In equation (3), the kinetic  $CO_2$  dependence is contained in the rate coefficient,  $k_0$ . The product inhibition raises the intrinsic  $CO_2$  dependence to the 1/2 power, hence the intrinsic  $CO_2$  dependence is first order, i.e.:

$$r_{CO} = k' p_{CO_2} p_{H_2O}^{-1} \quad (4)$$

The similar behaviour under light and dark conditions indicates that fundamental reaction mechanisms under photochemical and thermochemical conditions are similar. This type of rate law produces an observed half order dependence on  $CO_2$  therefore based on our analysis the reaction has a first order dependence on the partial pressure of  $CO_2$ .

The effective order of reaction for  $H_2$  is determined by measuring the reaction rate while varying the partial pressure of  $H_2$  and keeping the total flow rate and the  $CO_2$  partial pressure constant. Figure 3C shows that the CO production rate, under dark reaction conditions, has almost no dependence on the  $H_2$  partial pressure. However, under light conditions, there appears to be a slight dependence (to the one-third power) of the CO production on the  $H_2$  partial pressure. This subtle difference may provide some insight into the effect of light on the mechanism. A deeper examination of this effect will be the subject of a future study. Nevertheless, this result provides additional support to the RWGS reaction mechanism proposed in later in Section 3.5.

### 3.3 Experimental DRIFTS Data

In order to identify surface species present during experimental conditions, in-situ DRIFTS measurements are carried out on the  $In_2O_{3-x}(OH)_y$  nanocrystals to identify the presence and/or absence of surface species under reaction conditions. These observations can be compared with the predicted surface species predicted by theory in Section 3.5. Prior to the spectroscopic studies, the  $In_2O_{3-x}(OH)_y$  nanocrystal powder is heated in the environmental chamber to 130°C under flowing  $H_2$  to remove any water or surface organics as well as to replicate pre-treatments that the sample may be subjected to prior to catalytic measurements. After pre-treatment the reference spectrum is taken under flowing He at room temperature shown in Supplementary Fig. S3.

The surface make-up of carbon species is investigated by flowing  $CO_2$  at 10  $cm^3 min^{-1}$  at various temperatures from room temperature to 150°C which is shown by the series of DRIFTS spectra in Fig. 5A. The spectral region of interest lies within

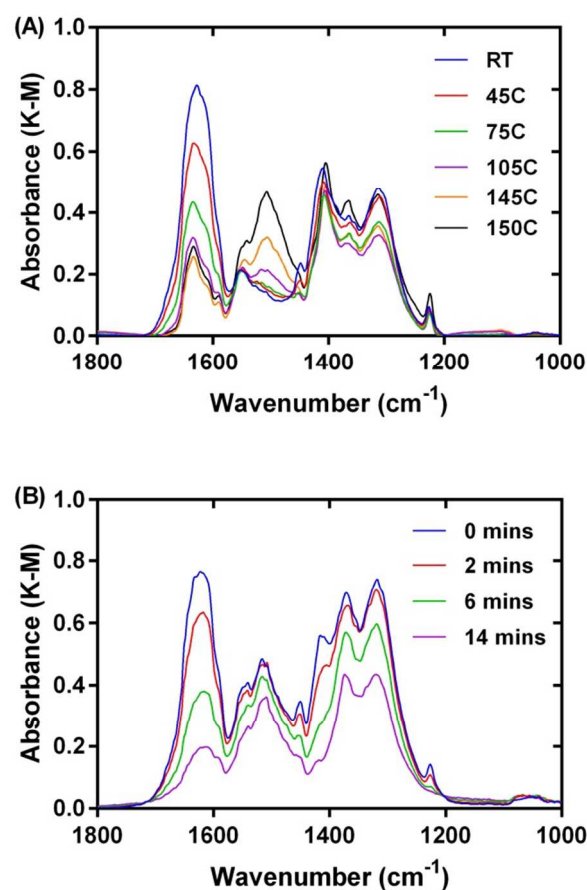


Fig. 5 *In-situ* DRIFTS spectra of  $In_2O_{3-x}(OH)_y$  nanocrystals under various atmospheres and temperatures. (A) Spectra measured during a temperature ramp from room temperature to 150°C under flowing  $CO_2$ . (B) Time dependent spectra measured during a He flush at room temperature following flowing  $CO_2$ .

1000 to 1800  $\text{cm}^{-1}$  which is characteristic of the stretching modes for carbon-based species. A bicarbonate species is identified by comparing the measured and fingerprint stretching modes (in brackets): the  $\delta(\text{OH})$  observed at 1224  $\text{cm}^{-1}$  (1220  $\text{cm}^{-1}$ ), the asymmetric stretch  $\nu_{\text{as}}(\text{CO}_3)$  observed at 1630  $\text{cm}^{-1}$  (1655  $\text{cm}^{-1}$ ) and the symmetric stretch  $\nu_{\text{s}}(\text{CO}_3)$  observed at 1406  $\text{cm}^{-1}$  (1405  $\text{cm}^{-1}$ ).<sup>41</sup> The bicarbonate peaks have the highest intensity at room temperature and decrease with increasing temperature. Since these peaks change in unison, it suggests that they represent the same species. The presence of this species is consistent with theoretical calculations, which predict a loosely bound bicarbonate species on the oxygen vacancy surface and is expected from other theoretical studies that show it is energetically favourable on this surface.<sup>31</sup>

Additional carbon species are observed at all temperatures in the measured range. A carbonate species is identified by comparing the measured and fingerprint stretching modes (in brackets): the asymmetric carbonate stretch  $\nu_{\text{as}}(\text{CO}_3)$  observed at 1546  $\text{cm}^{-1}$  (1550  $\text{cm}^{-1}$ ) and the symmetric carbonate stretch  $\nu_{\text{s}}(\text{CO}_3)$  observed at 1320  $\text{cm}^{-1}$  (1309  $\text{cm}^{-1}$ ). A formate species is also observed, with lower signal intensities, by comparing the measured and fingerprint stretching modes (in brackets): 1590  $\text{cm}^{-1}$  (1567  $\text{cm}^{-1}$ ) 1406  $\text{cm}^{-1}$  (1377  $\text{cm}^{-1}$ ) and 1367  $\text{cm}^{-1}$  (1366  $\text{cm}^{-1}$ ).

In order to observe the relative strength of adsorption of the surface carbon species, the  $\text{In}_2\text{O}_{3-x}(\text{OH})_y$  nanocrystal powder is cooled to room temperature under flowing  $\text{CO}_2$  (10  $\text{cm}^3 \text{min}^{-1}$ ) after which the flowing gas is exchanged with flowing He (10  $\text{cm}^3 \text{min}^{-1}$ ) which is shown by the series of DRIFTS spectra in Fig. 5B. Within 14 minutes it is observed that the intensity for all surface carbon species decreases, most of which is the bicarbonate species, where the fingerprint mode for the bicarbonate  $\delta(\text{OH})$  disappears. Further investigation by heating to 150  $^\circ\text{C}$  under flowing He (10  $\text{cm}^3 \text{min}^{-1}$ ) continues the trend of decreasing intensity, however, no single species appears to stand out as more strongly adsorbed than another.

In order to observe the surface species under experimental reaction conditions, the sample is investigated under flowing  $\text{H}_2$  and  $\text{CO}_2$  at 20  $\text{cm}^3 \text{min}^{-1}$  total, at 150  $^\circ\text{C}$ . During this experiment light, guided via an optic fibre, irradiated the sample. Under these conditions, we were unable to identify any surface species within the spectral region of interest between 1000 to 1800  $\text{cm}^{-1}$  because of the presence of an intense Drude absorption. This broad absorption peak has previously been observed on reduced indium oxide. However, it is observed that this peak is observed at high temperatures ( $>130^\circ\text{C}$ ) in flowing  $\text{H}_2$  as well as under irradiation without the presence of  $\text{H}_2$ . This may indicate that the accumulation of conduction band electrons in oxygen vacancies plays a role in the activity and  $\text{H}_2$  and light both influence their abundance.<sup>27</sup>

### 3.4 Fundamental RWGS mechanism from DFT calculations

In order to gain an atomic scale understanding of the fundamental reaction pathway of the RWGS reaction on

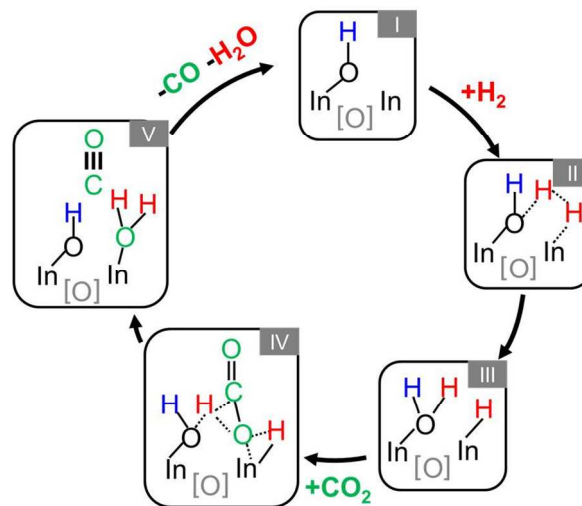


Fig. 6 Overall proposed mechanism for the  $\text{CO}_2 + \text{H}_2 \rightarrow \text{CO} + \text{H}_2\text{O}$  reaction on  $\text{In}_2\text{O}_{3-x}(\text{OH})_y$ .

$\text{In}_2\text{O}_{3-x}(\text{OH})_y$ , in-depth theoretical calculations were performed. We first describe the overall reaction mechanism deduced from DFT simulations, by analysing active sites for different crystal surfaces described below. Thereafter, we evaluate reaction pathways and activation energy barriers for key steps in the overall reaction. Experimental observations supporting the theoretically proposed mechanism are further discussed in Section 3.5. In Fig. 6 we show the fundamental reaction mechanism for the RWGS reaction over  $\text{In}_2\text{O}_{3-x}(\text{OH})_y$  obtained through DFT simulations by studying the interaction of  $\text{CO}_2$  and  $\text{H}_2$  with pristine and hydroxylated and oxygen containing surfaces (Fig. 7).

We begin with the study of the oxygen deficient surface, considering 9 possible oxygen vacancy sites labelled as O1 to O9 shown in Fig. 1E. It was found that the vacancy formation at all sites is endothermic in nature (vacancy formation energies are tabulated in Table S2 of Supporting Information). The theoretical results identified the O1 vacancy (O1-vac) site to be the most favourable owing to its smallest formation energy, while the O4 vacancy (O4-vac) site was determined as the least favourable. These observations are consistent with previous understanding.<sup>42</sup> The optimized  $\text{In}_2\text{O}_{3-x}$  surface (having O4-vac) is shown in Fig. 7C. In order to mimic experimental conditions where surface hydroxide groups were present, one lattice oxygen from the  $\text{In}_2\text{O}_3$  (111) surface was then substituted by an OH group (Stage I, Fig. 6). For this analysis, two possible sites for OH were considered, corresponding to the most favourable oxygen vacancy site (O1-vac) and the least favourable one (O4-vac). DFT computations showed that OH binds very strongly to the In atom near either of O1-vac and O4-vac sites with seemingly little difference between the binding energies at two sites (-2.76 eV at the O4-vac site and -2.71 eV at the O1-vac site). Furthermore, the nature of bonding showed that OH was bound terminally with In for both sites. Fig. 7E shows the optimized configuration of the resultant hydroxylated  $\text{In}_2\text{O}_3$ .

$x(\text{OH})_y$  surface having O4-vac substituted by OH group. In this process, the neighboring In of the O4 site that bonded with OH showed a slight increase in its positive charge, indicating the transfer of its excess electrons to O of OH. However, the other neighboring In of the O4 site, without an OH group, showed a slight decrease in its usual positive charge with respect to the lattice O. This unique spatial arrangement of atoms created by replacing lattice O with OH in proximity to In, results in the formation of Lewis acid-base pairs on the surface of  $\text{In}_2\text{O}_3$ .  $x(\text{OH})_y$  and is probably responsible for activating and dissociating  $\text{H}_2$  heterolytically, as discussed below. The transfer of excess surface electrons from In to the O of the OH is further evident from the molecular orbital description illustrated in Fig. S5 contained in the Supporting Information. Here it can be seen that the excess charge present in the highest occupied molecular

orbital (HOMO) of the  $\text{In}_2\text{O}_{3-x}$  surface (Fig. S5B) due to the oxygen vacancy becomes neutralized in the presence of the OH group (Fig. S5C). The theoretical calculations also indicated that the least favorable oxygen vacancy site (O4-vac) produced strong OH binding suggesting that less favorable sites for oxygen vacancies on  $\text{In}_2\text{O}_3$  may be able to bind surface hydroxides readily in search for a more stable configuration.

The role of the  $\text{H}_2$  molecule was investigated next (stages II and III in Fig. 6), by studying its adsorption on the  $\text{In}_2\text{O}_3$ .  $x(\text{OH})_y$  surface having OH substituting lattice oxygen at the least (O4-vac) and the most (O1-vac) stable oxygen vacancy sites. The results showed that  $\text{H}_2$  becomes adsorbed molecularly on both sites exothermally. The surface having OH substitution to O4-vac site was found to be particularly interesting wherein  $\text{H}_2$  undergoes endothermic heterolytic splitting (see Supporting

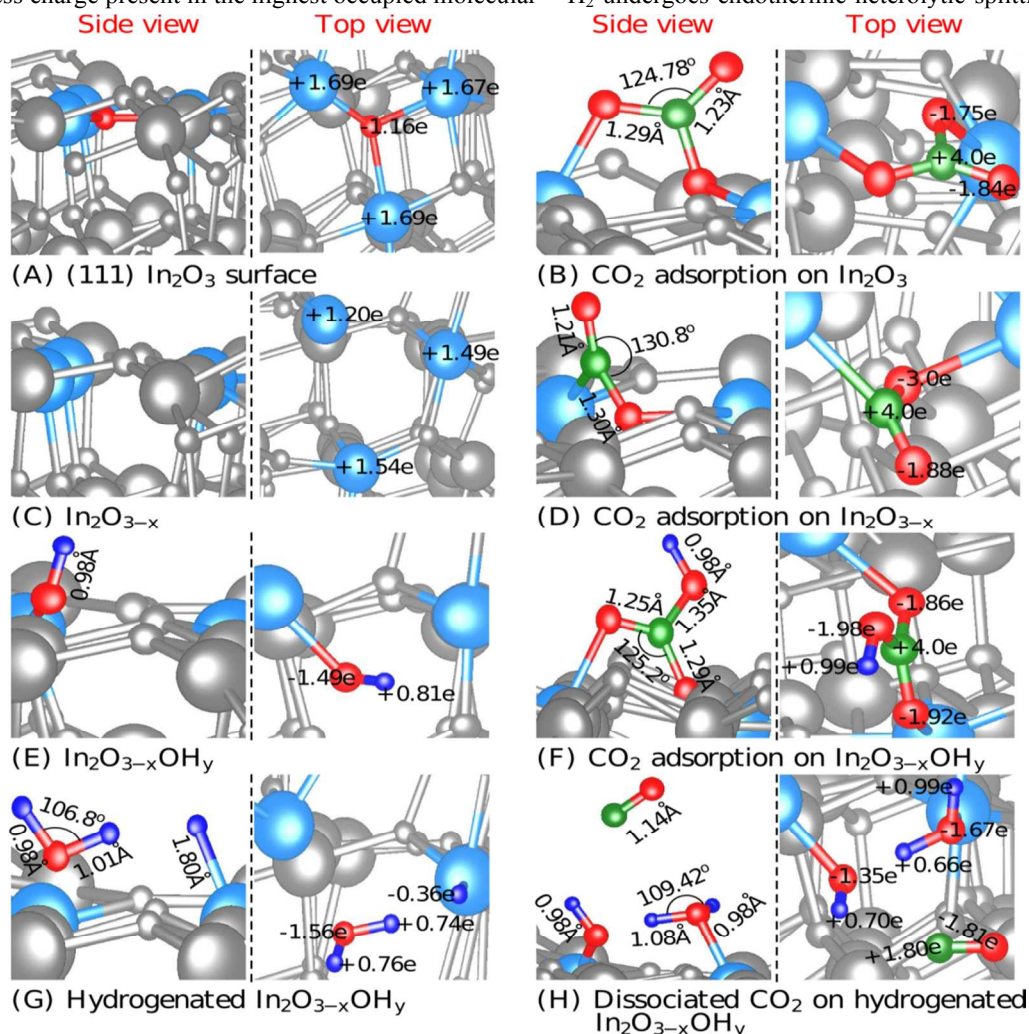


Fig. 7 Side and top view of optimized configurations for (A) pristine (111)  $\text{In}_2\text{O}_3$  surface, (B) adsorbed  $\text{CO}_2$  on pristine surface, (C)  $\text{In}_2\text{O}_3$  surface with O vacancy (O4-vac) defect ( $\text{In}_2\text{O}_{3-x}$ ), (D)  $\text{In}_2\text{O}_{3-x}$  surface with adsorbed  $\text{CO}_2$  molecule, (E)  $\text{In}_2\text{O}_{3-x}$  surface with OH in place of O4 site ( $\text{In}_2\text{O}_{3-x}(\text{OH})_y$ ), (F)  $\text{In}_2\text{O}_{3-x}(\text{OH})_y$  surface with adsorbed  $\text{CO}_2$  molecule, (G) hydrogenated  $\text{In}_2\text{O}_{3-x}(\text{OH})_y$  surface, and (H)  $\text{CO}_2$  reduction on hydrogenated  $\text{In}_2\text{O}_{3-x}(\text{OH})_y$  surface. Surface In, O, H and C atoms participating in the reaction are highlighted in light blue, red, dark blue and green, respectively. All other In and O atoms are represented by big and small grey balls, respectively. Side view represents bond lengths and bond angles while top view represents Bader charges of atoms participating in  $\text{CO}_2$  reduction reaction.

Information Table S5), during the absorption process. This results in proton binding to the surface O of the OH group and a hydride binding to the adjacent In site leading to formation of new In-H and H-OH bonds. The relaxed structure for the hydrogenated  $\text{In}_2\text{O}_{3-x}(\text{OH})_y$  surface is shown in Fig. 7G. Bader charge analysis reveals that the Lewis acidic In and Lewis basic O of the OH sites at the surface possess charges of  $+1.66e$  and  $-1.50e$  respectively, and generate a strong electric field on the outer surface that polarizes the  $\text{H}_2$  molecule as it approaches the surface. This is evident from Bader charges for H in stage II of Fig. 6, ( $-0.34e$  and  $+0.39e$ ), which suggest strong polarization of the H-H bond leading to the stabilization of structure. This charge analysis thus favours the heterolytic dissociative adsorption of  $\text{H}_2$  on the  $\text{In}_2\text{O}_{3-x}(\text{OH})_y$  surface. Because H is more electronegative than In the H atom of the  $\text{H}_2$  molecule nearest to the In atom accepts the excess charge from Lewis acid In and thereafter attains a negative effective charge of  $-0.36e$ , forming what can be best described as a hydride. On the other hand, as O is more electronegative than H, the other H atom of the  $\text{H}_2$  molecule loses its electrons to the Lewis base O of the OH and attains a positive effective charge of  $+0.74e$ , thereby forming what is in essence a proton. The newly formed In-H and H-OH bonds have lengths of  $1.80 \text{ \AA}$  and  $1.01 \text{ \AA}$  respectively, with the stable H-OH structure (Fig. 7G) having bond angle ( $106.8^\circ$ ) similar to that of water. Overall, our analysis shows that the formation of Lewis acid-base pairs may account for the heterolytic dissociation of  $\text{H}_2$  on the  $\text{In}_2\text{O}_{3-x}(\text{OH})_y$  surface.

In order to investigate the role of surface hydroxides and oxygen vacancies on the  $\text{CO}_2$  reduction reaction, we conducted an analysis for  $\text{CO}_2$  adsorption on pristine  $\text{In}_2\text{O}_3$  (Fig. 7B),  $\text{In}_2\text{O}_{3-x}$  (Fig. 7D) and  $\text{In}_2\text{O}_{3-x}(\text{OH})_y$  (Fig. 7F) surfaces. Again, multiple unique adsorption sites (on either the In or O atoms) of the pristine (111) surface as shown in Fig. 1E were considered. None of the In sites labelled as In1 to In7 showed any appreciable chemical reactivity for  $\text{CO}_2$  adsorption, whereas most of the O sites were able to interact with  $\text{CO}_2$  when it was placed close to the surface atoms. This is as expected due to the higher electronegativity of surface O atoms which can share charge with the C atom as opposed to In surface atoms.  $\text{CO}_2$

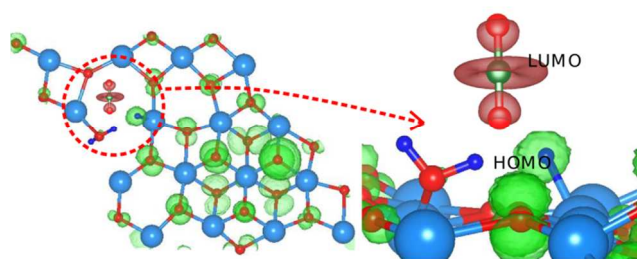


Fig. 8 Highest occupied molecular orbital (HOMO) of the (111) terminated  $\text{In}_2\text{O}_{3-x}(\text{OH})_y + 2\text{H}^*$  surface and lowest unoccupied molecular orbital (LUMO) of  $\text{CO}_2$  molecule. Red, light blue, dark blue and green balls represent O, In, H and C atoms, respectively.

gets adsorbed on the O5 site (Fig. 7B) with negative  $\Delta H_{\text{ads}}$ . Upon  $\text{CO}_2$  adsorption, the charge on the nearest surface O atom increases, while the two O atoms in the  $\text{CO}_2$  molecule experience corresponding decreases in effective charge. This results in a bending of the  $\text{CO}_2$  molecule. Nonetheless, the adsorption energies of  $\text{CO}_2$  on the pristine  $\text{In}_2\text{O}_3$  surface were found to be extremely weak (Table S1 in Supporting Information), suggesting the improbability of  $\text{CO}_2$  reduction on  $\text{In}_2\text{O}_3$  catalysts without surface hydroxides and oxygen vacancies.

The  $\text{CO}_2$  adsorption on the  $\text{In}_2\text{O}_{3-x}$  surface was investigated. A careful analysis of multiple  $\text{CO}_2$  placement strategies, over the least and most favourable vacancy sites showed that the only O vacant site that demonstrated some level of interaction with  $\text{CO}_2$  was the one having the least favorable O vacancy, O4-vac (binding energies are tabulated in Table S3 in Supporting Information). Interaction of  $\text{CO}_2$  with the  $\text{In}_2\text{O}_{3-x}$  surface having O4-vac leads to bending of the molecule (bond angle  $130.8^\circ$ ) and elongation of carbon-oxygen bonds to  $1.21 \text{ \AA}$  and  $1.30 \text{ \AA}$  (Fig. 7D).  $\text{CO}_2$  interaction with this site as

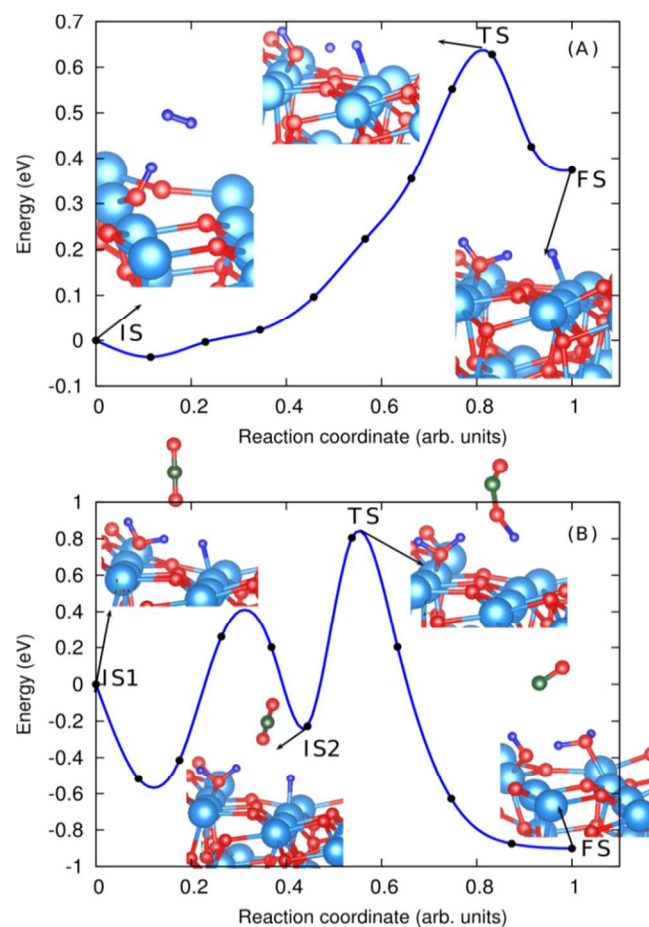


Fig. 9 Reaction pathway and energy barrier of (A)  $\text{H}_2$  dissociation on  $\text{In}_2\text{O}_{3-x}\text{OH}_y$  and (B)  $\text{CO}_2$  dissociation on  $\text{In}_2\text{O}_{3-x}\text{OH}_y + 2\text{H}^*$  surfaces, from Climbing Image Nudged Elastic Band (CI-NEB) method. Red, light blue, dark blue and green balls represent O, In, H and C atoms, respectively.

compared to the O1-vac site is likely due to the availability of relatively higher energy surface electrons.

Subsequently, we investigated CO<sub>2</sub> adsorption on the In<sub>2</sub>O<sub>3-x</sub>(OH)<sub>y</sub> surfaces with O1-vac and O4-vac oxygen vacancies. DFT computations showed that only the In<sub>2</sub>O<sub>3-x</sub>(OH)<sub>y</sub> surface with the O4-vac and a vertical orientation of CO<sub>2</sub> produce a slightly negative adsorption energy (see Supporting Information Table S4). The bond angle of the initially linear CO<sub>2</sub> molecule becomes 125.2° and the two C-O bond lengths increase to 1.25 Å and 1.29 Å, respectively, as shown in Fig. 6F. It was found that the O of CO<sub>2</sub> interacts with surface In atoms when it is adsorbed at the O4-vac site having OH bonded to its neighboring In. Bader charge analysis shows that the oxygen of CO<sub>2</sub> gets attracted towards excess electrons created by the O vacancy, whereas the oxygen atom of the OH molecule acts as an electrophile and shares electrons with the C atom. This leads to a decrease in electrons on the oxygen's of CO<sub>2</sub>, which further enables them to interact with surface In atoms. The energetically favored state of CO<sub>2</sub> interacting with In<sub>2</sub>O<sub>3-x</sub>(OH)<sub>y</sub> in the ground state can be described as a tridentate form of adsorbed CO<sub>2</sub> (Fig. 7F). On the other hand, the configurations that showed weak interaction of CO<sub>2</sub> with In<sub>2</sub>O<sub>3</sub> at the O5 site and In<sub>2</sub>O<sub>3-x</sub> at the O4-vac site, had both O and C atoms of CO<sub>2</sub> interacting with the surface (In, O) atoms to generate a bi-dentate carbonate-like species as shown in Figs. 7B and 7D, respectively.

Lastly, the adsorption of CO<sub>2</sub> on the In<sub>2</sub>O<sub>3-x</sub>(OH)<sub>y</sub> surface in the presence of H<sub>2</sub> was studied (stages IV and V in Fig. 6). This simulation most closely resembles the RWGS experimental conditions reported above. ΔH<sub>ads</sub> calculations for multiple configurations of CO<sub>2</sub> placement, showed that a CO<sub>2</sub> molecule cannot be stably adsorbed on the hydrogenated In<sub>2</sub>O<sub>3-x</sub>(OH)<sub>y</sub> surface with OH substituting the O1 site.

On the other hand the hydrogenated In<sub>2</sub>O<sub>3-x</sub>(OH)<sub>y</sub> surface with OH in place of the O4 site produced negative ΔH<sub>ads</sub> as well as the bending of CO<sub>2</sub> for most of the configurations we considered. The most interesting configuration that lead to the bending as well as dissociation of the CO<sub>2</sub> molecule is the one where CO<sub>2</sub> was inserted in the In-H bond, shown in stage IV of Fig. 6. Here, both O and C atoms of CO<sub>2</sub> interact with the surface (In, O and H) atoms to generate a bi-dentate species (Fig. 7H). This initial configuration made the structure highly unstable because of repulsion between the proton and the electrophilic C and the hydride and nucleophilic O of CO<sub>2</sub>. This configuration first leads to formation of a formate like complex which finally dissociates into CO and H<sub>2</sub>O, (stage V, Fig. 6) exothermically. The newly formed H<sub>2</sub>O molecule has O-H bond lengths of 1.08 and 0.98 Å and a bond angle of 109.4°, which is in fact very close to that of water in its ground state. The initially released CO molecule has a C-O bond length slightly higher (0.012 Å) than it has in its ground state. Bader charge analysis showed that the hydride formed after heterolytic splitting of H<sub>2</sub> lost its negative charge after the CO<sub>2</sub> adsorption. Furthermore, the two H atoms which originally were formed due to heterolytic dissociation of the H<sub>2</sub> molecule and had become strongly oppositely charged hydride and

proton, now both displayed positive charges of +0.66e and +0.99e as part of the newly formed H<sub>2</sub>O molecule (Fig. 7H). The C and O atoms of the released CO were found to possess roughly equal positive (+1.80e) and negative (-1.81e) effective charges, respectively, maintaining overall charge neutrality. The dissociative chemisorption of CO<sub>2</sub> can be further understood from Fig. 8 where the orbital interaction between the LUMO of CO<sub>2</sub> and the HOMO of the In<sub>2</sub>O<sub>3-x</sub>(OH)<sub>y</sub> surface with dissociated H<sub>2</sub> is shown. The HOMO of the surface consists of not only surface oxygen atoms but also the orbitals from the nucleophilic hydride with a symmetry that matches the LUMO of CO<sub>2</sub>, which is an anti-bonding σ\* orbital. Charge transfer from the surface to CO<sub>2</sub> occurs due to this HOMO-LUMO overlap, leading to the dissociation of CO<sub>2</sub>.

In order to evaluate the minimum energy pathway for the reaction and get a sense of the relative activation energy barriers faced during dissociation of H<sub>2</sub> and CO<sub>2</sub> molecules, CI-NEB calculations were performed. In order to capture the energetics of the molecular diffusion and adsorption process, the molecules were initially placed at a sufficient distance (~3.5 Å) above the surface. These calculations showed that H<sub>2</sub> dissociation on In<sub>2</sub>O<sub>3-x</sub>(OH)<sub>y</sub> surface is endothermic with an activation energy barrier of 0.66 eV (see Fig. 9A). It can be seen from the figure that H-H bond breaking from the initial state (IS) to the transition state (TS) mainly contributes to the activation energy barrier of H<sub>2</sub> dissociation.

The exothermic dissociation of CO<sub>2</sub> on the hydrogenated In<sub>2</sub>O<sub>3-x</sub>(OH)<sub>y</sub> surface has an activation barrier of 1.03 eV along with an additional activation barrier of 0.77 eV. In Fig. 9B, IS1 shows the initial state with an undistorted CO<sub>2</sub> molecule. IS2 shows a secondary state higher in energy than the first in which the geometry of the CO<sub>2</sub> molecule is slightly distorted. The small barrier in this transformation corresponds to the energy required for orientation and distortion from the linear geometry of CO<sub>2</sub> molecule as it approaches the surface. Further, the high activation energy barrier of CO<sub>2</sub> dissociation suggests that this is the difficult step in the reaction mechanism and thus the rate determining step. This is consistent with first order dependence of the production rate on the partial pressure of CO<sub>2</sub> deduced from experimental observations.

To summarize the theoretical observations, this extensive DFT analysis has demonstrated that a In<sub>2</sub>O<sub>3-x</sub>(OH)<sub>y</sub> surface containing both Lewis base hydroxide groups and Lewis acid indium sites together with oxygen vacancies can heterolytically dissociate H<sub>2</sub> to form a hydride bonded to In and a proton bonded to a lattice O. This hydrogenated In<sub>2</sub>O<sub>3-x</sub>(OH)<sub>y</sub> surface facilitates CO<sub>2</sub> reduction by mediating charge transfer between the In<sub>2</sub>O<sub>3-x</sub>(OH)<sub>y</sub> surface and adsorbed reactants CO<sub>2</sub> and H<sub>2</sub> to form CO and H<sub>2</sub>O products, which subsequently desorb from the surface.

### 3.5 Reverse water gas shift reaction on In<sub>2</sub>O<sub>3-x</sub>(OH)<sub>y</sub>

The mechanism we propose for the RWGS reaction on the (111) surface of In<sub>2</sub>O<sub>3-x</sub>(OH)<sub>y</sub> can be described by a series of reaction steps as follows: In the first step (Eq. 5), H<sub>2</sub> undergoes

heterolytic dissociation into a hydridic In-H and a protonic O-H surface site. In the second step (Eq. 6), CO<sub>2</sub> adsorbs at an active site comprised of an oxygen vacancy, an indium hydride and a proton on a hydroxide group that causes CO<sub>2</sub> to dissociate to CO with the concomitant formation of H<sub>2</sub>O. This is followed by desorption of the reaction products CO and H<sub>2</sub>O, represented by reaction (Eq. 7) and (Eq. 8):



In the overall reaction oxygen vacancies and hydroxide groups are not consumed, instead they work synergistically to assist in the production of an active site that facilitates the heterolytic splitting of H<sub>2</sub>, which is then capable of promoting the dissociation of CO<sub>2</sub> into CO. In this reaction scheme, gas phase CO<sub>2</sub> reacts directly with a preformed hydrogenated active site, instead of first adsorbing on an adjacent surface site and forming a reaction intermediate which subsequently reacts.

This type of reaction can be described using classical Eley-Rideal type kinetics, where a gas phase species reacts directly with an adsorbed species. For this type of kinetic scheme it is generally observed that there is a first order dependence of the gas phase reacting species on the overall rate of reaction. Based on the experimental kinetic investigations, it is observed that the reaction order with respect to CO<sub>2</sub> is one half. The space velocity dependence and preliminary DFT analysis of CO<sub>2</sub> adsorption in presence of H<sub>2</sub>O revealed that it is likely that a reaction product is inhibiting, which is most likely H<sub>2</sub>O, since it can block CO<sub>2</sub> adsorption at surface active hydroxyl and oxygen vacancy sites.<sup>43</sup> In this case, it was demonstrated previously that a first order dependence on CO<sub>2</sub> is possible with an inhibiting reaction product. Therefore, the experimental results are consistent with the theoretically derived mechanism.

*In-situ* DRIFTS analysis was conducted to observe surface carbon species in an attempt to identify reactant, intermediate and product species under various reaction conditions. Bicarbonate, carbonate and formate groups were identified on the surface, however it is not clear if they are bystander species, if they are involved in CO<sub>2</sub> adsorption or if they are an intermediate species. The DFT analysis predicted that the adsorbed CO<sub>2</sub> surface species are weakly bonded to the surface. The relative strength of adsorption can be evaluated by flushing the chamber with flowing He (at 10 cm<sup>3</sup> min<sup>-1</sup>) at room temperature after flowing CO<sub>2</sub> (at 10 cm<sup>3</sup> min<sup>-1</sup>). The time dependent removal of adsorbed CO<sub>2</sub> species upon the switch from flowing CO<sub>2</sub> to He is shown in the DRIFT spectra in Fig. 5B. Within 15 minutes there is a significant decrease among the peaks identified as being a bicarbonate-like species. In our previous study, it was established that In<sub>2</sub>O<sub>3-x</sub>(OH)<sub>y</sub> adsorbed CO<sub>2</sub>, suggesting that the more strongly adsorbed species is a possibly captured as a carbonate or formate and not as a bicarbonate.<sup>28</sup> The collected experimental and theoretical

results of this study demonstrate that the thermochemical and photochemical RWGS reaction depends on the concentration of available surface hydroxide groups and oxygen vacancies.

The DFT calculations also showed the dependence of the CO<sub>2</sub> reduction reaction on active sites present on the surface. Thus CO<sub>2</sub> was not able to dissociate on an In<sub>2</sub>O<sub>3-x</sub>(OH)<sub>y</sub> surface alone. However, it does dissociate on In<sub>2</sub>O<sub>3-x</sub>(OH)<sub>y</sub> in the presence of hydrides and protons formed from heterolytic dissociation of H<sub>2</sub> and this happens favourably, with a small energy barrier, when CO<sub>2</sub> is present in close proximity to the hydrogenated In<sub>2</sub>O<sub>3-x</sub>(OH)<sub>y</sub> surface. Further, no dissociation of CO<sub>2</sub> was observed in the absence of surface hydrides even if O vacancies and OH groups are present and CO<sub>2</sub> is in vicinity of these defects.

### 3.6 Frustrated Lewis Pair Surfaces

Frustrated Lewis pairs (FLPs) are obtained when a main group Lewis acid and Lewis base are combined without forming a “classical” Lewis acid-base adduct but instead leave the acidity and basicity unquenched due to the steric bulk of their substituents. The FLP remained a chemical curiosity until Stephan and co-workers discovered their unique reactivity.<sup>44</sup> They found that FLPs were able to activate small molecules, where the unquenched nature of such Lewis pairs results in the observation of unusual and important chemical reactivity.<sup>45</sup>

Especially worth mentioning in the context of the mechanism described in this paper, are the observations that molecular FLPs can induce the heterolytic cleavage of H<sub>2</sub>, reversible binding and release of CO<sub>2</sub>, and reduction of CO<sub>2</sub>, for example to CO.<sup>46</sup> These FLPs represent the only non-transition metal based systems known for this type of hydrogen activation and reaction chemistry.

What we find especially fascinating is the analogous relationship of the reactivity of molecular FLPs with H<sub>2</sub> and CO<sub>2</sub> to similar kinds of surface chemical reactions that we have discovered in the work described herein for In<sub>2</sub>O<sub>3-x</sub>(OH)<sub>y</sub> nanomaterials with H<sub>2</sub> and CO<sub>2</sub>. Like molecular FLPs, In<sub>2</sub>O<sub>3-x</sub>(OH)<sub>y</sub> also has main group Lewis acid-base proximal sites, the terminal hydroxide acts as a Lewis base and the indium acts as Lewis acid (as shown in steps II and III in Fig. 6), a connection which bodes well for the future development of a new class of “FLP heterogeneous catalysts” that among many reaction possibilities could enable efficient gas-phase hydrogenation chemistry of CO<sub>2</sub> to fuels and chemicals.

The archetypical design of a FLP heterogeneous catalyst introduced in this paper represents an important first step towards the realization of the artificial leaf. However, to close the gap from science to technology through FLP heterogeneous catalysts, key questions remain to be answered. Although our preliminary TD-DFT simulations suggest that the overall process of CO<sub>2</sub> reduction on a defective hydroxylated surface analyzed in this study still applies in the excited state, the details of the mechanism such as the optical transitions and the rate-limiting step in the presence of light are currently being

investigated. The role of surface FLPs on catalytic processes in the presence of light is also an open question for now. Once we develop a fundamental understanding of surface FLPs, it would be highly desirable to optimize the selection of Lewis acid and Lewis base surface sites, their concentration and chemical and physical characteristics so as to achieve the best reaction efficiency. It can be clearly seen that these are complex questions that would require significant new studies requiring synergistic integration of experimental and theoretical efforts, which can be made possible by collaborative efforts between scientists working in this area. Experimental work is currently underway to investigate the effect of light on the FLP sites during the heterolytic cleavage of H<sub>2</sub>. Our ongoing and future investigations will focus on answering these questions.

#### 4.0 Conclusions

This work represents the first combined experimental and theoretical attempt to understand the mechanism of the RWGS reaction on the surface of In<sub>2</sub>O<sub>3-x</sub>(OH)<sub>y</sub> nanocrystals in the dark and light. The collected findings provide a valuable insight into the role, that surface hydroxide groups and oxygen vacancies play, in the thermochemical and photochemical activation of H<sub>2</sub> and CO<sub>2</sub> reactants to form CO and H<sub>2</sub>O products. The rate limiting step for both the light and dark reactions is the dissociation of CO<sub>2</sub>. Additionally, it appears that the light and dark reactions proceed via similar pathways based on similar reaction orders for the reactants. The relationship between heterolytic dissociation of H<sub>2</sub> and reduction of CO<sub>2</sub> on molecular FLPs and our similar observations on the surface of In<sub>2</sub>O<sub>3-x</sub>(OH)<sub>y</sub> nanocrystals may herald the birth of the new field of FLP heterogeneous catalysis. Based on the results and with the insight gained from this work, it should prove possible to design new single-component nanostructured materials and improve upon existing ones through rational chemistry control of the composition, size, shape, surface and assembly of nanomaterials and thereby improve the conversion efficiency of CO<sub>2</sub> reduction to energy rich fuels. Furthermore, by understanding the mechanism by which these materials activate CO<sub>2</sub>, these systems can be incorporated into multi-component systems such as the artificial leaf, combining both water splitting and CO<sub>2</sub> reduction. To fully understand the function of light on the RWGS reaction, further experimental and theoretical studies are currently under way.

#### Acknowledgements

GAO is Government of Canada Research Chair in Materials Chemistry and Nanochemistry. This work was supported by the Natural Sciences and Engineering Research Council of Canada (NSERC), the University of Toronto, Ontario Ministry of Research and Innovation (MRI) and the Ontario Ministry of Economic Development and Innovation (MEDI). Computations were performed at SciNet<sup>28</sup> and Calcul Quebec consortia under

the auspices of Compute Canada. SciNet is funded by the Canada Foundation for Innovation, the Government of Ontario, Ontario Research Fund - Research Excellence, and the University of Toronto. The authors gratefully acknowledge the strong and sustained support of all the above organizations. Detailed discussions of the design of the flow reactor with Professor Cathy Chin were invaluable to this work. In-situ spectroscopy was done with the gracious help of Dongmin Yun and Professor Jorge Luis Gabayet Dominguez at the University of Western Ontario. Critical reading and appraisal of this manuscript and insightful discussions with Professors Douglas Stephan and Robert Morris are also deeply appreciated.

#### Notes and references

<sup>a</sup> Department of Materials Science and Engineering, University of Toronto, 184 College Street, Suite 140, Toronto, Ontario, M5S 3E4, Canada, [chandaveer.singh@utoronto.ca](mailto:chandaveer.singh@utoronto.ca).

<sup>b</sup> Department of Chemical Engineering and Applied Chemistry, University of Toronto, 200 College Street, Suite 103, Toronto, Ontario, M5S 3E4, Canada, [charles.mims@utoronto.ca](mailto:charles.mims@utoronto.ca).

<sup>c</sup> Department of Chemistry, University of Toronto, 80 St. George St., Suite 326, Toronto, Ontario, M5S 3E4, Canada, Email: [gozin@chem.utoronto.ca](mailto:gozin@chem.utoronto.ca).

† These authors contributed equally to this work.

Electronic Supplementary Information (ESI) available: [details of any supplementary information available should be included here]. See DOI: 10.1039/b000000x/

#### References

- 1 N. S. Lewis and D. G. Nocera, *Proc. Natl. Acad. Sci.*, 2006, **103**, 15729–15735.
- 2 M. Hambourger, G. F. Moore, D. M. Kramer, D. Gust, A. L. Moore and T. A. Moore, *Chem. Soc. Rev.*, 2009, **38**, 25–35.
- 3 G. a Olah, A. Goepfert and G. K. S. Prakash, *J. Org. Chem.*, 2009, **74**, 487–98.
- 4 Z. Jiang, T. Xiao, V. L. Kuznetsov and P. P. Edwards, *Philos. Trans. A. Math. Phys. Eng. Sci.*, 2010, **368**, 3343–64.
- 5 G. F. Moore and G. W. Brudvig, *Annu. Rev. Condens. Matter Phys.*, 2011, **2**, 303–327.
- 6 D. G. Nocera and M. P. Nash, *Proc. Natl. Acad. Sci.*, 2006, **103**, 15729–15735.
- 7 G. Centi, E. A. Quadrelli and S. Perathoner, *Energy Environ. Sci.*, 2013, **6**, 1711.
- 8 J. a Herron, J. Kim, A. Upadhye, G. Huber and C. T. Maravelias, *Energy Environ. Sci.*, 2014.
- 9 G. A. Olah, A. Goepfert and G. K. S. Prakash, *J. Org. Chem.*, 2009, **74**, 487–498.

- 10 S. Bensaid, G. Centi, E. Garrone, S. Perathoner and G. Saracco, *ChemSusChem*, 2012, **5**, 500–521.
- 11 S. N. Habisreutinger, J. K. Stolarczyk and O. Semiconductors, *Angew. Chem. Int. Ed. Engl.*, 2013, **52**, 7372–408.
- 12 K. Mori, H. Yamashita and M. Anpo, *RSC Adv.*, 2012, **2**, 3165.
- 13 H. Yamaura, T. Jinkawa, J. Tamaki, K. Moriya, N. Miura and N. Yamazoe, *Sensors Actuators B Chem.*, 1996, **36**, 325–332.
- 14 H. Lorenz, W. Jochum, B. Klötzer, M. Stöger-Pollach, S. Schwarz, K. Pfäller and S. Penner, *Appl. Catal. A Gen.*, 2008, **347**, 34–42.
- 15 S. Sato, *J. Photochem. Photobiol. A Chem.*, 1988, **45**, 361–367.
- 16 S. . Poznyak, a. . Golubev and a. . Kulak, *Surf. Sci.*, 2000, **454-456**, 396–401.
- 17 T. Bielz, H. Lorenz, W. Jochum, R. Kaindl, F. Klausner, B. Klötzer and S. Penner, *J. Phys. Chem. C*, 2010, **114**, 9022–9029.
- 18 P. P. Edwards, A. Porch, M. O. Jones, D. V. Morgan and R. M. Perks, 2004, 2995–3002.
- 19 C. G. Granqvist and a. Hultåker, *Thin Solid Films*, 2002, **411**, 1–5.
- 20 A. Walsh, J. Da Silva, S.-H. Wei, C. Körber, a. Klein, L. Piper, A. DeMasi, K. Smith, G. Panaccione, P. Torelli, D. Payne, a. Bourlange and R. Egdell, *Phys. Rev. Lett.*, 2008, **100**, 167402.
- 21 P. King, T. Veal, F. Fuchs, C. Wang, D. Payne, a. Bourlange, H. Zhang, G. Bell, V. Cimalla, O. Ambacher, R. Egdell, F. Bechstedt and C. McConville, *Phys. Rev. B*, 2009, **79**, 205211.
- 22 G. Thomas, *Drug Alcohol Rev.*, 1998, **17**, 471–480.
- 23 T. Koida and M. Kondo, *J. Appl. Phys.*, 2006, **99**, 1–7.
- 24 a. Bourlange, D. J. Payne, R. G. Egdell, J. S. Foord, P. P. Edwards, M. O. Jones, a. Schertel, P. J. Dobson and J. L. Hutchison, *Appl. Phys. Lett.*, 2008, **92**, 3–6.
- 25 E. H. Morales and U. Diebold, *Appl. Phys. Lett.*, 2009, **95**, 5–8.
- 26 O. Bierwagen, M. E. White, M. Y. Tsai and J. S. Speck, *Appl. Phys. Lett.*, 2009, **95**, 2007–2010.
- 27 K. H. L. Zhang, D. J. Payne, R. G. Palgrave, V. K. Lazarov, W. Chen, a. T. S. Wee, C. F. McConville, P. D. C. King, T. D. Veal, G. Panaccione, P. Lacovig and R. G. Egdell, *Chem. Mater.*, 2009, **21**, 4353–4355.
- 28 L. B. Hoch, T. E. Wood, P. G. O'Brien, K. Liao, L. M. Reyes, C. a. Mims and G. a. Ozin, *Adv. Sci.*, 2014, n/a–n/a.
- 29 J. P. Perdew, K. Burke and M. Ernzerhof, *Phys Rev Lett*, 1996, **77**, 3865.
- 30 A. M. Rappe, K. M. Rabe, E. Kaxiras and J. D. Joannopoulos, *Phys. Rev. B*, 1990, **41**, 1227–1230.
- 31 P. Giannozzi, S. Baroni, N. Bonini, M. Calandra, R. Car, C. Cavazzoni, D. Ceresoli, G. L. Chiarotti, M. Cococcioni, I. Dabo and others, *J. Phys. Condens. Matter*, 2009, **21**, 395502.
- 32 K. H. L. Zhang, A. Walsh, C. R. A. Catlow, V. K. Lazarov and R. G. Egdell, *Nano Lett.*, 2010, **10**, 3740–3746.
- 33 R. F. W. Bader and P. J. MacDougall, *J. Am. Chem. Soc.*, 1985, **107**, 6788–6795.
- 34 G. Henkelman, A. Arnaldsson and H. Jónsson, *Comput. Mater. Sci.*, 2006, **36**, 354–360.
- 35 G. Mills, H. Jonsson and G. K. Schenter, *Surf. Sci.*, 1995, **324**, 305–337.
- 36 H. Jonsson, G. Mills and K. W. Jacobsen, *World Sci.*, 1998, **Singapore**.
- 37 G. Henkelman and H. G. Jonsson, *J Chem Phys*, 2000, **113**, 9978.
- 38 X. Fu, L. a. Clark, W. a. Zeltner and M. a. Anderson, *J. Photochem. Photobiol. A Chem.*, 1996, **97**, 181–186.
- 39 B. Ohtani, *Phys. Chem. Chem. Phys.*, 2014, **16**, 1788–97.
- 40 A. a. Upadhye, I. Ro, X. Zeng, H. J. Kim, I. Tejedor, M. a. Anderson, J. a. Dumesic and G. W. Huber, *Catal. Sci. Technol.*, 2014.
- 41 G. Busca and V. Lorenzelli, *Mater. Chem.*, 1982, **7**, 89–126.
- 42 A. Walsh, *Appl. Phys. Lett.*, 2011, **98**, 261910.
- 43 T. Bielz, H. Lorenz, P. Amann, B. Klötzer and S. Penner, *J. Phys. Chem. C*, 2011, **115**, 6622–6628.
- 44 G. C. Welch, R. R. San Juan, J. D. Masuda and D. W. Stephan, *Science*, 2006, **314**, 1124–1126.
- 45 D. W. Stephan and G. Erker, *Angew. Chemie - Int. Ed.*, 2010, **49**, 46–76.
- 46 G. C. Welch and D. W. Stephan, *J. Am. Chem. Soc.*, 2007, **129**, 1880–1881.